

New evidence for dark matter

A. Boyarsky^{1,2}, O. Ruchayskiy¹, D. Iakubovskiy², A.V. Macciò³, D. Malyshev⁴

¹Ecole Polytechnique Fédérale de Lausanne,
FSB/ITP/LPPC, BSP CH-1015, Lausanne, Switzerland

²Bogolyubov Institute for Theoretical Physics,
Metrologichna str., 14-b, Kiev 03680, Ukraine

³Max-Planck-Institut für Astronomie, Königstuhl 17, 69117 Heidelberg, Germany

⁴Dublin Institute for Advanced Studies, 31 Fitzwilliam Place, Dublin 2, Ireland

Observations of star motion, emissions from hot ionized gas, gravitational lensing and other tracers demonstrate that the dynamics of galaxies and galaxy clusters cannot be explained by the Newtonian potential produced by visible matter only [1–4]. The simplest resolution assumes that a significant fraction of matter in the Universe, dominating the dynamics of objects from dwarf galaxies to galaxy clusters, does not interact with electromagnetic radiation (hence the name *dark matter*). This elegant hypothesis poses, however, a major challenge to the highly successful Standard Model of particle physics, as it was realized that dark matter cannot be made of known elementary particles [4]. The quest for direct evidence of the presence of dark matter and for its properties thus becomes of crucial importance for building a fundamental theory of nature. Here we present a new universal relation, satisfied by matter distributions at all observed scales, and show its amazingly good and detailed agreement with the predictions of the most up-to-date *pure dark matter* simulations of structure formation in the Universe [5–7]. This behaviour seems to be insensitive to the complicated feedback of ordinary matter on dark matter. Therefore, it potentially allows to compare theoretical predictions directly with observations, thus providing a new tool to constrain the properties of dark matter. This work extends the previous analysis [8–10] to a larger range of masses, demonstrates a different scaling law, and compares it with numerical simulations. Such a universal property, observed in structures of all sizes (from dwarf spheroidal galaxies to galaxy clusters), is difficult to explain without dark matter, thus providing new evidence for its existence.

Current cosmological data, including the earliest stage of structure formation, are well-described by the “concordance model” (Λ CDM) [11]. The microscopic properties of the dark matter particles can strongly affect the formation of cosmic structures, originating from tiny perturbations in the primordial density field. Within the Λ CDM the dark matter is assumed to be non-interacting and to have no primordial velocity – *cold dark matter* (CDM). To describe the formation and properties of virialized DM objects at a later, non-linear, stage of structure formation, numerical N-body simulations have been extensively used [12]. It was demonstrated that within the CDM model spherically averaged density profiles of DM halos of all scales are self-similar and universal [13, 14].

Many works have addressed the issue of measuring the DM distribution in observed objects (see e.g. [1–3, 15–17]). Two classes of profiles have been used to fit observational data: profiles with singular, cusp-like behaviour at small radii r (e.g. NFW profile [13]) or profiles that tend to a constant central density ρ_c – *cored profiles*, such as e.g. pseudo-isothermal profile [18] (ISO) or Burkert profile [15] (BURK). Both profile families are described by two basic parameters: a characteristic scale r_* at which the inner slope of the DM density profile changes towards its outer asymptotic and an average density ρ_* within this radius.

Unfortunately current data do not allow us to determine, in a conclusive way, the presence of cores or cusps in the observed density distributions. Often the same data set can be equally well fitted by profiles of different type [16, 17, 19–21]. The deviation from predictions of pure CDM models can occur for several reasons: for example, a significant influence of baryons; the microscopic properties of dark matter particles different from those of CDM (non-gravitational self-interaction or interaction with baryons, non-zero primordial velocities). Moreover baryons can contribute significantly (and may even dominate) the total mass profile in the inner regions, and thus pure CDM predictions are difficult to test.

Recently the works [9, 10] analysed rotation curves and weak lensing data for a sample of dwarf, spiral and elliptical galaxies fitted by the Burkert profile and demonstrated that the mean dark matter surface density $\langle \Sigma \rangle = \rho_* r_*$ remains constant for all these galaxies. In this work we extend the analysis of [9, 10] to galaxies and galaxy clusters. We have compiled a catalog of DM distribution in various celestial objects from more than 50 scientific publications. After applying uniform selection criteria to this catalog (see **Method summary**), we were left with 805 Dark Matter profiles (490 NFW, 285 ISO and 30 BURK) from 289 unique objects: 124 spiral galaxies, 11 dwarf spheroidals (dSphs), 10 elliptical galaxies, 25 galaxy groups and 121 galaxy clusters. To properly compare DM distributions, fitted by different density profiles, we introduce a *dark matter column density*, averaged over the central part of an object:

$$\mathcal{S} = \frac{2}{r_*^2} \int_0^{r_*} r dr \int dz \rho_{\text{DM}}(\sqrt{r^2 + z^2}) \simeq \frac{M_{\text{cyl}}}{\pi r_*^2}, \quad (1)$$

Integral over z extends to the virial boundary of a DM halo. The definition (1) implies that \mathcal{S} is proportional to the dark matter surface density within r_* ($\mathcal{S} \propto \rho_* r_*$). For distant objects \mathcal{S} is defined via M_{cyl} – mass within a cylinder of radius r_* . Parameters of different profiles that fit the same DM density distribution are related (for example, r_s for NFW is equal to $6.1r_c$ for ISO and equals to $1.6r_B$ for BURK). Choosing these values as r_* in each case, one finds that the value of \mathcal{S} for NFW (cuspy profile with r^{-3} asymptotic at large radii) and ISO (cored profile with r^{-2} behaviour at large scales) differ by less than 10% (the difference between NFW and BURK is $\sim 2\%$), see Supporting Information for details. Thus, the DM column density \mathcal{S} is *insensitive to the type of DM density profile, used to fit the same observational data*.

Our final dataset spans more than four orders of magnitude in r_* ($0.2 \text{ kpc} \lesssim r_* \lesssim 2.5 \text{ Mpc}$) and about eight orders of magnitude in halo masses.¹ The observational data can be fit by a single power-law:

$$\lg \mathcal{S} = 0.21 \lg \frac{M_{\text{halo}}}{10^{10} M_{\odot}} + 1.79 \quad (2)$$

(with \mathcal{S} in $M_{\odot} \text{ pc}^{-2}$). One could try to interpret the data presented in Fig. 1 in spirit of [8–10] (i.e. $\mathcal{S} = \text{const}$), although with a higher value of $\mathcal{S} \approx 260 M_{\odot} \text{ pc}^{-2}$ (as was originally suggested in [22]). The apparent trend at higher masses could then be attributed to systematic errors and observational bias. Indeed, the results are based on observational data of different nature and different quality and we do not consider in this work observational errors. However, both M_{halo} and \mathcal{S} were computed, using 3 density profiles on average, which should diminish the errors. The scaling relation (2) is supported by the data, spread over many orders in magnitude in halo mass, and the shift of some data points should not significantly affect the systematic trend.

Next, we compare our data with outcomes from cosmological N-body simulations within the Λ CDM model [6, 7]. For each simulated halo we compute M_{halo} , fit the particle distribution to the NFW density profile and calculate \mathcal{S} using formula (1). The observational data together with results from Λ CDM numerical simulations [6] is plotted of the Fig. 1. The black dashed-dotted line on this Figure is the $\mathcal{S} - M_{\text{halo}}$ relation obtained from N-body simulations [6], using the WMAP fifth year [11] cosmological parameters. It fairly well reproduces the fit (2). Moreover, the pink shaded region (showing the 3σ scatter

¹We use M_{200} as halo mass M_{halo} . A proper definition of M_{200} can be found e.g. in [6] or in the Supplementary Information.

in the simulation data) contains most of the observational points within the halo mass range, probed by simulations. Therefore, the observed $M_{\text{halo}} - \mathcal{S}$ scaling coincides with the relation between the parameters of DM density profiles observed in numerical simulations for long time [5,6,13] over more than five orders of magnitude in mass.

Dwarf spheroidal satellites (dSphs) of the Milky Way (orange diamonds on the Fig. 1) do not follow the relation (2). Recently the Aquarius project has produced a statistically significant sample of well resolved density profiles for satellite halos [7], making it possible to determine their $r_* - \rho_*$ relation. Satellites were found to be more concentrated than isolated halos and thus have a higher value of \mathcal{S} at fixed M_{halo} . Fig. 1 shows that the $\mathcal{S} - M_{\text{halo}}$ relation for satellite halos (gray dashed line) from the Aquarius simulation [7] reproduces well the data on dSphs.

The fit to the data without the dSphs has the slope ≈ 0.23 , much better quality of fit, and coincides extremely well with the results of N-body simulations [6] for isolated halos (black dashed-dotted line on Fig. 1). At masses below $10^{10} M_{\odot}$ no isolated halos were resolved in [6] and a simple toy model [6,23] was used to predict the relation between parameters of NFW profile in a given cosmological scenario. The model (dotted line in the Fig. 1) fits well the results for the few spiral galaxies in this range. *Thus the agreement between observations and predictions from Λ CDM extend over more than eight orders of magnitude in mass.*

Comparison of our data with theoretical predictions (N-body simulations in our case) indicates that, despite the presence of various systematic errors in the data, the DM distributions in the observed objects exhibit a universal property – a systematic change of the average column density \mathcal{S} as a function of the object mass ($\mathcal{S} \propto M_{\text{halo}}^{0.2}$, relation (2)). This is different from the flat $\mathcal{S} = \text{const}$ dependence, previously suggested [8–10]. The latter is based, in our view, on a confusion between the properties of isolated and non-isolated halos. Excellent agreement with pure DM simulations suggest also that the observed scaling dependence is insensitive to the presence of baryons, details of local environment, formation history.

The relation (2) can be used to search for deviations from CDM model (e.g. warm DM models [24]) or modifications of gravity at large scales [25]. This motivates dedicated astronomical observations with all the data processed in a uniform way. Studies of the galaxies with the masses below $10^{10} M_{\odot}$ and galaxy clusters would be especially important.

Various scaling relations are known in astrophysics (“fundamental plane relation” for elliptical galaxies [26], “Tully-Fisher relation” for spiral galaxies [27], etc.). The relation discussed in this Letter differs in one crucial aspect: *it extends uniformly to all classes of objects at which DM is observed*. It would be very difficult to explain such a relation within Modified Newtonian dynamics [28] theory considered as an alternative to DM. That is why this relation, further confirmed, studied and understood analytically, may serve as one more evidence of the existence of Dark Matter.

If DM particle posses a radiative *decay* channel (as predicted by several particle physics models), a possible signal in X-ray or γ -ray observations would be proportional to the DM column density averaged within the instrument’s field-of-view. It then follows from our analysis that decaying DM would produce a unique all-sky signal, with a known slow-varying angular distribution. Such a signal can be easily distinguished from any possible astrophysical background and therefore makes the astrophysical search for decaying DM *another type of a direct detection experiment* [22,29,30].

Method summary

We collected from the literature 1095 DM density profiles for 357 unique objects ranging from dSphs to galaxy clusters. For each DM profile found in our sample we have applied uniform selection criteria:

- If for an object several independently determined profiles were available and all of them but one agreed in the values of r_* and ρ_* within a factor of 5, we rejected the outlier.
- For some objects the best-fit value of the characteristic radius r_* was extrapolated well outside the

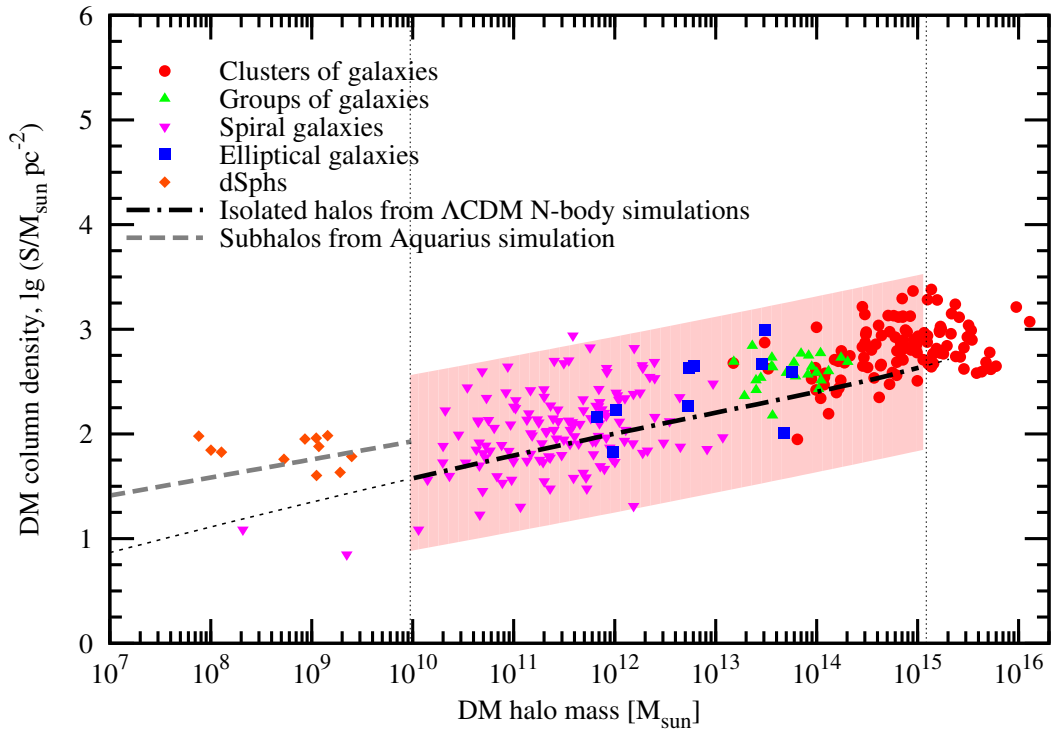


Figure 1: **Column density \mathcal{S} as a function of halo mass M_{halo} .** The black dashed-dotted line is the $\mathcal{S} - M_{\text{halo}}$ relation obtained from N-body simulations [6], using the WMAP fifth year cosmological parameters [11]. The shaded region shows the 3σ scatter in the simulation data. The vertical lines indicate the mass range probed by simulations. The dotted line is the theoretical prediction from the toy model for isolated halos [6, 23]. The gray dashed line shows the results from the Aquarius simulation for satellite halos [7].

region covered by the observational data, R_{data} . In this case the parameters of the density profile had extremely large uncertainties. We have thus rejected objects with $r_* < 2.75R_{\text{data}}$.

- We rejected profiles for which the uncertainty in any quoted parameter (r_* or ρ_*) was higher than a factor of 10.
- For objects with more than one profile selected, the average value of \mathcal{S} and M_{halo} was used in the subsequent analysis.
- When processing the data of N-body simulations we used the fit of particle distribution by the NFW density profile and computed \mathcal{S} , using equation (1).
- If *the same* observational data is fit by several different DM profiles (e.g. NFW, ISO, and BURK), one can then find a relation between characteristic scales r_* and densities ρ_* of these profiles. Provided such a relation holds, the difference between the column densities \mathcal{S}_{NFW} , $\mathcal{S}_{\text{BURK}}$ and \mathcal{S}_{ISO} turns out to be less than 10%. Qualitatively, this can be understood as follows: to explain the same velocity data, two DM profiles should have roughly the same mass within some radius R_0 . If both profiles happen to have the same behaviour at large distances, their \mathcal{S} values, averaged over R_0 will be essentially equal. This explains the use of \mathcal{S} as a characteristic of DM halos.

Supplementary information is presented in the Appendix.

Acknowledgments. Numerical simulations were performed on the PIA and on the PanStarrs2 clusters of the Max-Planck-Institut für Astronomie at the Rechenzentrum in Garching. D. I. is grateful to Scientific and Educational Centre of the Bogolyubov Institute for Theoretical Physics in Kiev, Ukraine, and especially to V. Shadura, for creating wonderful atmosphere for young Ukrainian scientists. The work of D. I. is supported from the ‘‘Cosmomicrophysics’’ programme, the Program of Fundamental Research of the Physics and Astronomy Division of the National Academy of Sciences of Ukraine, and from the grant No. F/16-417-2007 of the Governmental Fund of Fundamental Research of the National Academy of Sciences of Ukraine. The work of O.R. was supported in part by the Swiss National Science Foundation.

Author contribution. A.B. and O.R. suggested the project, contributed to analysing and interpreting the data, comparing them with numerical simulations, and writing the paper; D.I. and D.M. collected the data on DM distributions and contributed to interpreting it; A.M. performed numerical simulations, contributed to comparison of their results with the data, and contributed to writing the paper. Correspondence should be addressed to A.B. or O.R. (alexey.boyardsky,oleg.ruchayskiy@epfl.ch).

Supplementary Information

In this Supplementary Information Section we demonstrate that the average DM column density \mathcal{S} is independent on the choice of the particular DM density profile; provide more details about the sample that was used and its comparison with simulations.

A Relation between parameters of DM density profiles

In this work we concentrated on three popular choices for DM density profile $\rho(r)$. Numerical (N-body) simulations of the cold DM model have shown that the DM distribution in all relaxed halos can be fitted with the universal Navarro-Frenk-White (NFW) profile [13]:

$$\rho_{\text{NFW}}(r) = \frac{\rho_s r_s}{r(1 + r/r_s)^2} \quad (3)$$

parametrised by ρ_s and r_s . A more useful parametrization is in terms of the halo mass, M_{200} , and the concentration parameter, $c \equiv R_{200}/r_s$. Namely, R_{200} is the radius at which the average DM density is 200 times larger than the critical density of the universe ρ_{crit} . The halo mass M_{200} is the total mass of DM within this radius. The variables (ρ_s, r_s) and (M_{200}, c) are thus connected as follows:

$$\begin{aligned}\rho_s &= f(c)\rho_{\text{crit}} \\ r_s &= \left(\frac{3M_{200}}{800\pi\rho_{\text{crit}}c^3} \right)^{1/3} \\ f(c) &= \frac{200}{3} \frac{c^3}{\ln(c+1) - c/(c+1)}\end{aligned}\quad (4)$$

The equations (4) allow to determine $\mathcal{S} \propto r_*\rho_*$, knowing halo mass and concentration parameter M_{200}, c .

The Burkert profile [15] has been shown to be successful in explaining the kinematics of disk systems (e.g. [31]):

$$\rho_{\text{BURK}}(r) = \frac{\rho_B r_B^3}{(r_B + r)(r_B^2 + r^2)}.\quad (5)$$

Another common parametrization of cored profiles is given by the pseudo-isothermal profile [18]

$$\rho_{\text{ISO}}(r) = \frac{\rho_c}{1 + r^2/r_c^2}.\quad (6)$$

The quantity $\mathcal{S}(R)$ can be calculated analytically for all these choice of $\rho(r)$. For example, for the pseudo-isothermal profile one obtains:

$$\mathcal{S}_{\text{ISO}}(R) = \frac{2\pi\rho_c r_c^2}{R^2} \left[\sqrt{R^2 + r_c^2} - r_c \right].\quad (7)$$

For the NFW density distribution (3):

$$\mathcal{S}_{\text{NFW}}(R) = \frac{4\rho_s r_s^3}{R^2} \left[\frac{\arctan \sqrt{R^2/r_s^2 - 1}}{\sqrt{R^2/r_s^2 - 1}} + \log \left(\frac{R}{2r_s} \right) \right].\quad (8)$$

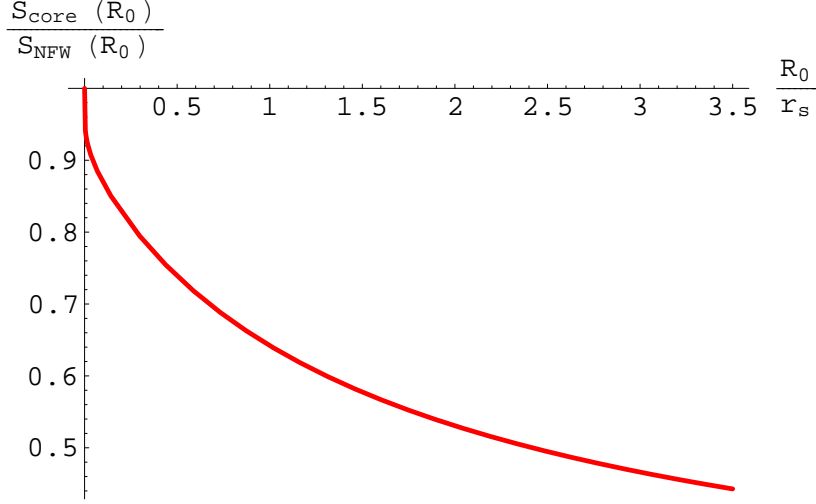
Notice, that this expression is real for both $R > r_s$ and $R < r_s$. The corresponding expression for the BURK is rather lengthy and not very illuminating.

A.1 Dependence of \mathcal{S} on the inner slope of density profile.

In order to equally well fit the same rotation curve data, two DM profiles should have roughly the same mass within some radius R_0 , determined by the observational data. If both profiles happen to have the same behaviour at large distances, their \mathcal{S} , averaged over R_0 will be essentially equal (as it is determined by the sum of the masses inside the sphere R_0 and in the outside of the cylinders, where the mass is dominated by the large r asymptotics).² In reality the situation is of course more complicated, one has to take into account the influence of baryons, the span of radii at which the data exists, etc.

We conservatively estimate the difference of column densities between a cusped and a cored profile as follows. We take the NFW density profile (3) as a representative of the cusped profile and its ‘‘extreme cored’’ counterpart $\rho_{\text{core}}(r)$ defined as follows:

$$\rho_{\text{core}}(r) = \begin{cases} \rho_{\text{NFW}}(r), & r > R_0 \\ \rho_{\text{NFW}}(R_0), & r \leq R_0 \end{cases}.\quad (9)$$



Supplementary Figure 2: **The ratio of average column densities of the extreme cored and NFW profiles as a function of R_0** (c.f. Eq. (9)).

The column densities of these two profiles, averaged within R_0 , differ only because the initial mass inside a *sphere* with radius R_0 for the cored profile (9) diminishes as compared to the NFW case.

The resulting ratio of DM column densities is shown in the Supplementary Fig. 2 as a function of averaging radius R_0 . In particular, for $R_0 = r_s$ this ratio is 64%, for $R_0 = 2r_s$ it equals to 53% and for $R_0 = 3r_s$ it drops to 47%. This implies that the difference of DM column densities between the cusped (NFW) and the extreme version of the cored profile (9) is within 50% for realistic averaging radii R_0 (usually $R_0 \sim 1 - 3r_s$). This difference is small compared to the intrinsic scatter expected on a object by object basis and well below the observational uncertainties on the parameters describing the density profile. This makes \mathcal{S} a very robust quantity to compare observed properties of DM halos and results from numerical simulations and, consequently, test the prediction of the CDM model.

The rotation curve of a galaxy is often fitted by several DM profiles (e.g. ISO and NFW). Let us analytically establish the relation between parameters of several profiles, *fitting the same rotation curve*. To this we take an ISO density profile and generate according to it the circular velocity profile $v_c^2(r)$, with r in the range $r_c \lesssim r \lesssim 15r_c$.³ Then we fit these data using an NFW profile (see Fig. 3, left). We find the following relations between the parameters of the two profiles:

$$\text{NFW vs. ISO} \quad : \quad r_s \simeq 6.1 r_c \quad ; \quad \rho_s \simeq 0.11 \rho_c . \quad (10)$$

The corresponding rotation curves and density profiles are shown in Supplementary Fig. 3.

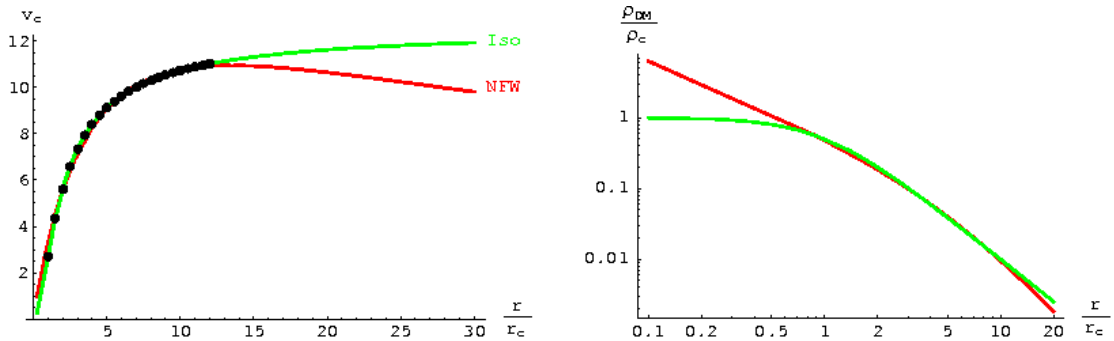
Let us now compare the column densities for NFW and ISO profiles, whose parameters are related via Eq. (10). Results as a function of radius R are shown on Fig. 4. In particular, one sees that for $R = r_s$

$$\frac{\mathcal{S}_{\text{NFW}}(r_s)}{\mathcal{S}_{\text{ISO}}(6r_c)} \approx 0.91 \quad . \quad (11)$$

One may be surprised that the cusped profile leads to the smaller column density than the cored one (as Eq. (11) demonstrate). This result however, can be simply understood. We match the velocity profiles for

²We will see below (Eq. (13)), that this is indeed the case for NFW and Burkert profiles.

³The final result is not sensitive to the exact choice of this range.



Supplementary Figure 3: **Comparison of NFW (red) and ISO (green) profiles for the simulated rotation velocity points.** *Left panel:* the velocity data (black points, in units of $G_N \rho_c r_c^2$) is generated, assuming the ISO profile and fitted with the NFW profile. The parameters of the corresponding NFW profile (in the units of r_c, ρ_c) are given by eq. (10) in the text. *Right panel:* comparison of the density profiles with parameters, related by (10). The x -axis is in the units of isothermal core radius r_c .

the NFW and ISO at some off-center distances $R_0 \sim 2r_s$, by demanding that the mass inside this sphere is the same for both profiles. The ISO profile is shallower in the outer regions than the NFW one. The ratio between the mass inside a sphere of the radius R_0 and a cylinder with base radius R_0 is equal to 0.58 at $R_0 = 6r_c$ for ISO profile, while it is 0.63 at $R_0 = r_s$ for the NFW profile. Thus the mass in the outer part of a cylinder is larger for the shallower ISO profile than for the cuspy NFW one, which explains the result (11).

It is clear from previous considerations that \mathcal{S}_{NFW} and $\mathcal{S}_{\text{BURK}}$ (similarly matched) should be essentially identical, as both profiles have identical behaviour at $r \rightarrow \infty$. Indeed, in the case of the NFW and Burkert profiles the relation between their characteristic parameters is given by

$$\text{NFW vs. BURK} \quad : \quad r_s \simeq 1.6r_B \quad ; \quad \rho_s \simeq 0.37\rho_B \quad (12)$$

which leads to

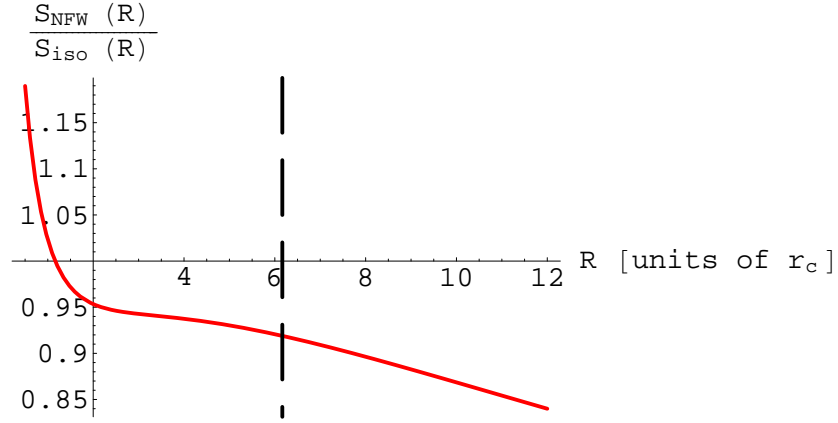
$$\frac{\mathcal{S}_{\text{NFW}}(r_s)}{\mathcal{S}_{\text{BURK}}(1.6r_s)} \approx 0.98 \quad . \quad (13)$$

Finally, it should be noticed that we assume an infinite extension for Dark Matter halos, when computing the column density. However, the integrals in (5) are convergent at large off-center distances and therefore the details of the truncation of the DM distributions for $R > R_{200}$ do not affect the value of \mathcal{S} by more than 10%.

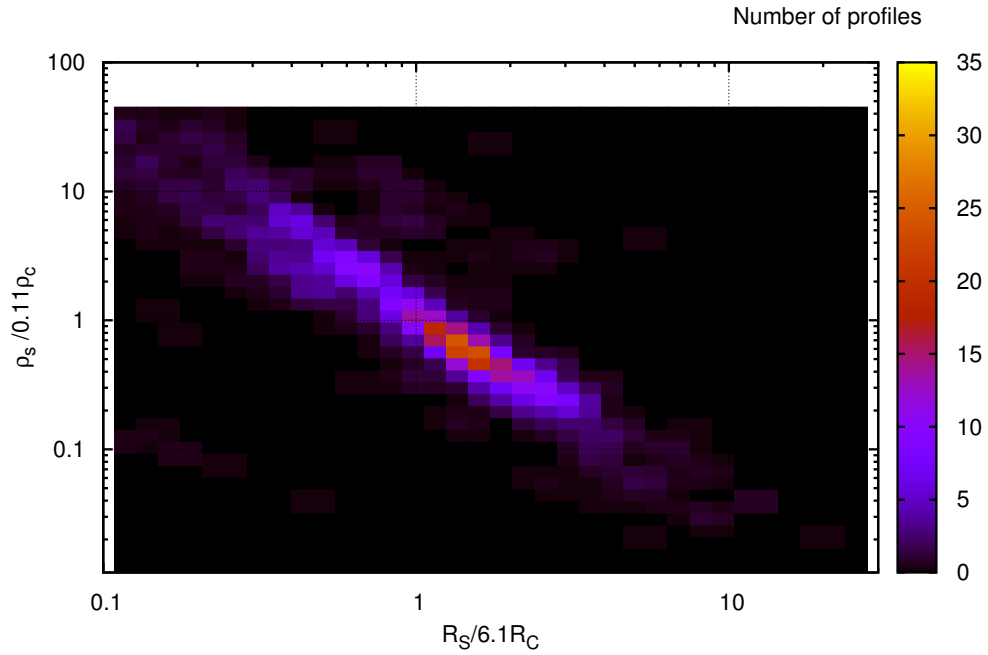
B Data analysis

We have collected from the literature 1095 DM profiles for 357 objects (from dwarf spheroidal galaxies to galaxy clusters, see Table 1 below). For each DM profile in our sample we have performed a number of checks. Those profiles that have not passed these checks were rejected from subsequent analysis. As a result of the selection process we were left with 805 DM profiles for 289 objects. The results of the selection are shown on the Supplementary Figure 6 below.

- When analysing the data, we realized that for some objects the value of r_* lies well outside the region covered by the observational data, R_{data} . Such objects systematically show extremely high values of



Supplementary Figure 4: **Comparison of the column densities of NFW and ISO profiles.** Profiles describe the same data and their parameters are related via (10). The column density is averaged within various radii R . Dashed vertical line marks $R = r_s = 6.1r_c$.



Supplementary Figure 5: **Relation between parameters of NFW and ISO profiles in observed objects.** For objects for which both NFW and ISO fits of velocity rotation curves were available, we plot the ratios r_s/r_c and ρ_s/ρ_c . The maximum of the histogram lies in a region (10).

r_* . For example, we found 37 galaxy profiles having $r_* > 100$ kpc, while their kinematic data usually extends only up to $R_{\text{data}} \sim 10 - 30$ kpc.

Therefore, we select only Dark Matter profiles having $r_* < 2.75R_{\text{data}}$. The coefficient 2.75 is justified by the following argument. The circular velocity in an NFW halo is given by

$$v_c^2(r) = \frac{G_N M_{\text{NFW}}(< r)}{r} = 4\pi G_N \rho_s r_s^3 \frac{\log(1 + \frac{r}{r_s}) - \frac{r}{r+r_s}}{r}. \quad (14)$$

For $r \ll r_s$ this function can be approximated as

$$v_c^2(r) \approx 2\pi G_N \rho_s r_s \left(r - \frac{4r^2}{3r_s} + \dots \right) \quad (15)$$

In the part of the velocity curve where $\frac{4r^2}{3r_s}$ is much less than the errors on the velocity dispersion one cannot reliably determine r_s and ρ_s (since $v_c^2(r)$ is indistinguishable from a straight line, proportional to $\rho_s r_s$). It is important to have data points in the region where the contribution of the quadratic term becomes noticeable to reliably extract both NFW parameters. We chose to set $2.75R_{\text{data}} \geq r_*$, which corresponds to a $\sim 50\%$ contribution from the second (quadratic) term to $v_c^2(r)$. Similar criteria are used for ISO and BURK profiles. This reduces the number of considered profiles from 1095 to 891.

- For 76 objects both NFW and ISO (or BURK) Dark Matter profiles were available. For these objects we checked the relation between the parameters of these profiles against the results shown in Eq. (10) (or Eq. (12) for BURK). Results of this comparison for the NFW and ISO profiles are shown in Fig. 5. This figure shows that there is indeed a maximum in the region defined by Eq. (10) but also that the scatter around this maximum is pretty large and that the difference between measured and expected ratios of NFW and ISO parameters can be as large as a factor of ten. Therefore we decided to exclude from our sample all objects with a ratio $\rho_s/\rho_c, r_s/r_c$, (or $\rho_s/\rho_B, r_s/r_B$ for BURK profiles) larger than a factor 5 with respect to the theoretical prediction shown in Eq. (10) or (12).
- Finally, in several cases parameters of DM density profiles were quoted with very large uncertainties. We decided to select only those profiles for which the ratio between the 1σ upper and lower bounds of quoted parameters (radius r_* or the density ρ_*) was smaller than a factor of 10.

To compare the $\mathcal{S} - M_{\text{halo}}$ relation for selected objects with N-body simulations, we used the results from [6]. This suit of Λ CDM numerical simulations probed the halo mass range $10^{10} - 10^{15} M_\odot$. For each simulated halo of [6] we computed M_{halo} , fit the particle distribution to the NFW density profile and calculate \mathcal{S} using Eqs.(4) and the definition (1). The observational data together with results from simulations is plotted of the Supplementary Figure 7. The small scatter of the simulation points at $M_{\text{halo}} \gtrsim 10^{14} M_\odot$ is explained by the finite size of the simulation box. The simulations with the large box size (e.g. [5]) verify that the scatter does not reduce at large masses (c.f. the pink shaded region on the Figure 1).

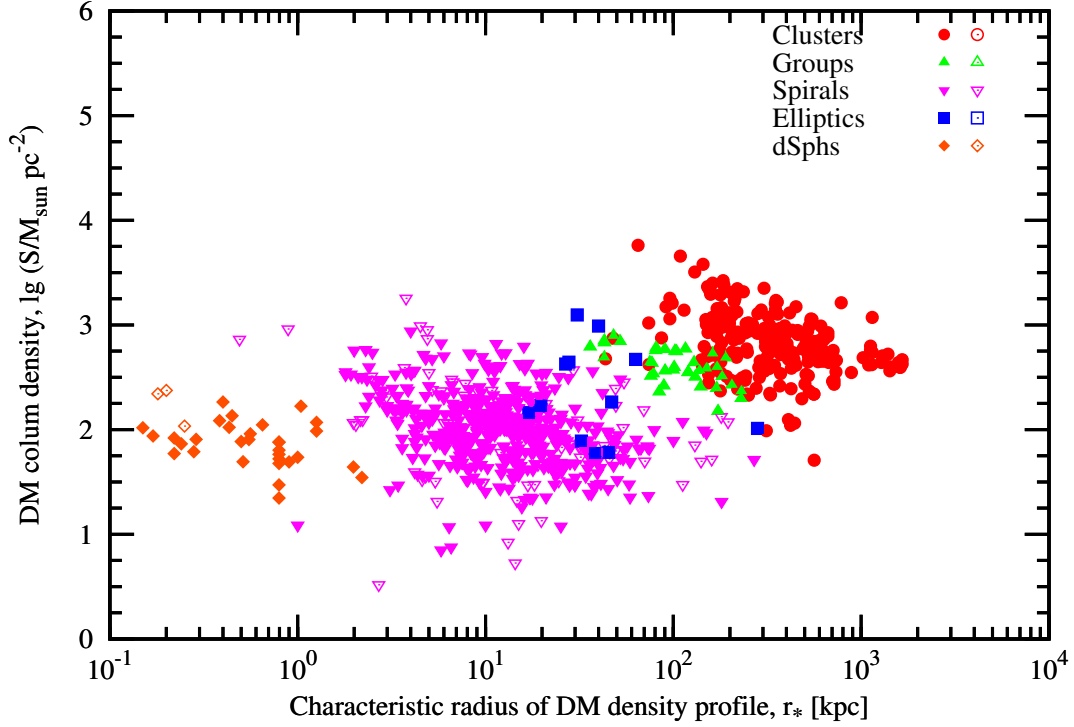
Supplementary Table 2: Halo mass M_{200} and DM column density \mathcal{S} for galaxy clusters.

Object name	$M_{200}[M_\odot]$	$\log_{10} \frac{\mathcal{S}}{M_\odot \text{ pc}^{-2}}$	Object name	$M_{200}[M_\odot]$	$\log_{10} \frac{\mathcal{S}}{M_\odot \text{ pc}^{-2}}$
2A 0335+096	1.44e+15	2.67	Abell 1068	5.64e+14	2.59
Abell 119	2.64e+15	2.74	Abell 133	4.35e+14	2.66
Abell 1367	6.89e+14	2.72	Abell 1413	9.87e+14	2.78
Abell 160	9.73e+13	2.63	Abell 1656 (Coma)	1.72e+15	3.01
Abell 168	3.19e+14	2.64	Abell 1689	1.56e+15	3.28
Abell 1703	1.25e+15	3.28	Abell 1763	9.92e+14	2.51

Clusters (continued on next page)

Object name	$M_{200} [M_{\odot}]$	$\log_{10} \frac{S}{M_{\odot} \text{ pc}^{-2}}$	Object name	$M_{200} [M_{\odot}]$	$\log_{10} \frac{S}{M_{\odot} \text{ pc}^{-2}}$
Abell 1795	1.76e+15	2.79	Abell 1835	1.27e+15	2.68
Abell 194	8.90e+13	2.53	Abell 1983	1.57e+14	2.39
Abell 1991	1.64e+14	2.69	Abell 2029	3.45e+15	2.90
Abell 209	5.26e+14	2.47	Abell 2142	5.98e+15	2.65
Abell 2199	9.57e+14	2.81	Abell 2204	7.24e+14	2.90
Abell 2218	7.88e+14	2.98	Abell 2219	1.65e+15	2.77
Abell 2256	3.84e+15	2.58	Abell 2319	4.75e+15	2.68
Abell 2390	1.54e+15	2.82	Abell 2537	8.18e+14	2.82
Abell 2597	2.94e+14	2.73	Abell 262	1.89e+14	2.68
Abell 2667	1.37e+15	2.64	Abell 267	1.74e+14	2.51
Abell 2717	1.66e+14	2.44	Abell 3112	2.84e+14	2.83
Abell 3266	5.17e+15	2.62	Abell 3376	2.13e+14	2.75
Abell 3526	9.84e+14	2.87	Abell 3562	9.33e+14	2.86
Abell 3571	5.17e+15	2.78	Abell 3627	1.43e+15	2.77
Abell 370	1.25e+15	2.88	Abell 383	6.19e+14	2.56
Abell 426	1.66e+15	2.97	Abell 478	1.42e+15	2.76
Abell 496	1.64e+15	2.99	Abell 511	9.21e+14	2.90
Abell 520	1.29e+16	3.07	Abell 539	2.83e+14	3.22
Abell 576	6.47e+14	3.12	Abell 611	7.43e+14	2.82
Abell 644	6.96e+14	2.72	Abell 68	3.71e+14	2.54
Abell 754	5.32e+15	2.62	Abell 780	9.96e+13	3.02
Abell 85	2.38e+15	2.74	Abell 851	9.85e+13	2.42
Abell 907	6.24e+14	2.79	Abell 963	6.78e+14	2.87
Abell S1101	1.76e+14	2.79	Abell S400	3.20e+15	3.04
Abell S540	1.69e+14	2.71	AC 114	1.27e+15	2.67
AWM 4	1.50e+14	2.71	CL 0016+1609	1.31e+14	2.19
CL 2244-0221	4.30e+14	2.65	CL J1226.9+3332	7.04e+14	3.29
B2002a 15	2.87e+14	2.65	MACS J0011.7-1523	1.14e+15	2.71
MACS J0159.8-0849	1.25e+15	2.94	MACS J0242.6-2132	5.28e+14	2.98
MACS J0329.7-0212	7.19e+14	2.86	MACS J0429.6-0253	4.11e+14	3.04
MACS J0744.9+3927	1.01e+15	2.93	MACS J0947.2+7623	1.16e+15	2.97
MACS J1115.8+0129	4.32e+15	2.59	MACS J1311.0-0311	6.72e+14	2.82
MACS J1411.3+5212	7.16e+14	3.13	MACS J1423.8+2404	5.79e+14	3.13
MACS J1427.6-2521	3.07e+14	2.95	MACS J1532.9+3021	9.40e+14	2.86
MACS J1621.6+3810	7.58e+14	2.99	MACS J1720.3+3536	9.67e+14	2.85
MACS J1931.8-2635	1.67e+15	2.78	MACS J2229.8-2756	3.10e+14	2.97
MKW 3S	1.10e+14	2.34	MKW 9	1.19e+14	2.54
MS 0015.9+1609	9.50e+15	3.21	MS 0116.3-0115	1.18e+14	2.47
MS 0302.7+1658	8.45e+14	3.12	MS 0451.6-0305	1.68e+15	3.03
MS 0735.6+7421	2.17e+15	3.15	MS 0839.9+2938	5.99e+14	2.93
MS 1006.0+1202	3.10e+15	2.93	MS 1008.1-1224	3.39e+15	2.99
MS 1137.5+6625	6.21e+14	2.69	MS 1224.7+2007	9.01e+14	3.37
MS 1358.4+6245	2.58e+15	3.12	MS 1455.0+2232	1.37e+15	3.38
MS 1512.4+3647	7.11e+14	3.12	MS 1910.5+6736	8.59e+14	2.80
MS 2137.3-2353	5.11e+14	3.13	PKS 0745-19	2.14e+15	2.96
PKS 0745-191	2.87e+15	2.82	RXC J0137.2-0911	9.83e+13	2.61
RXC J0454.8-1806	1.21e+14	2.58	RXC J1504.1-0248	1.95e+15	2.84
RX J0056.9-2740	6.45e+13	1.95	RX J0419.6+0225	3.06e+13	2.87
RX J0439.0+0520	4.39e+14	2.94	RX J0439.0+0521	3.85e+14	2.86
RX J1023.6+0411	2.88e+15	2.62	RX J1223.0+1037	3.31e+13	2.62
RX J1347.5-1145	2.36e+15	3.24	RX J1416.4+2315	3.00e+14	3.14
RX J1504.1-0248	1.80e+15	2.77	RX J2129.6+0005	7.15e+14	2.71
SDSS J1004+4112	3.02e+14	2.87	Triangulum	3.32e+15	2.91
Virgo	4.16e+14	2.35	ZWCL 0024.0+1652	3.49e+14	2.80
ZWCL 1321.4+1358	1.50e+13	2.68			

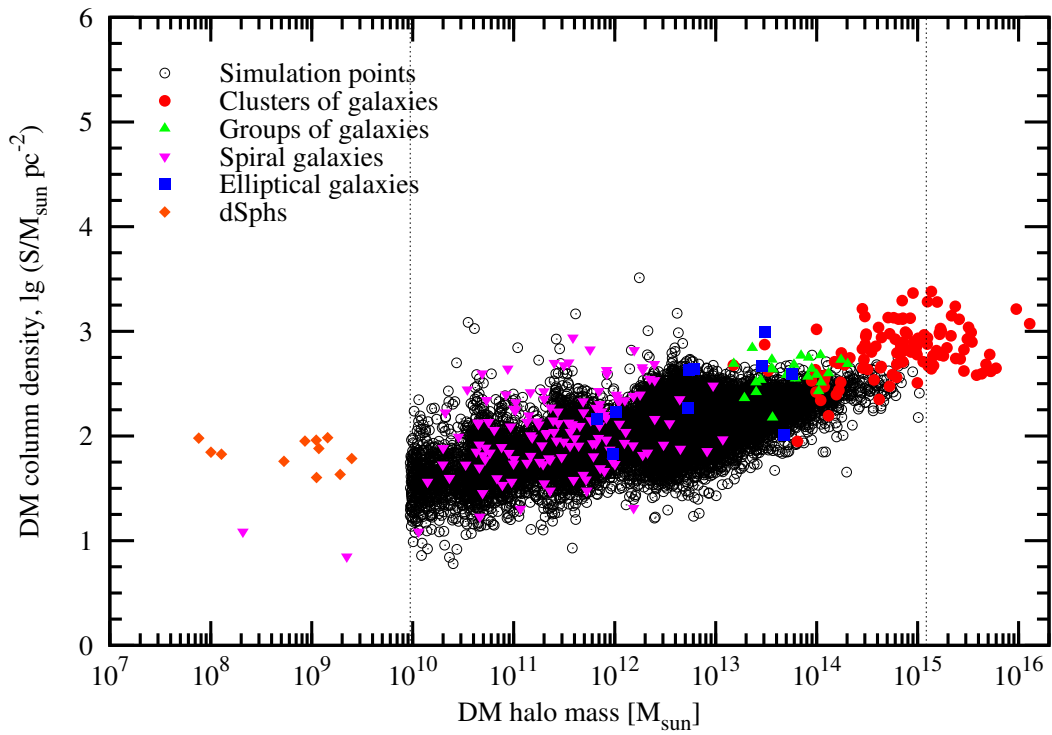
Clusters (end)



Supplementary Figure 6: **Selected DM density profiles.** DM column density S as a function of the characteristic radius r_* for 1095 *density profiles*. Filled (open) shapes denote accepted (rejected) density profiles, according to our selection criteria. Notice, that unlike Figure 1, an object may appear several times in this Figure if more than one profile was available.

Type	Number of objects	References	List of selected objects
Galaxy clusters	130	[32–44]	Table 2
Galaxy groups	26	[45–47]	Table 3
Elliptical galaxies	10	[48–52]	Table 4
Spiral galaxies	180	[18, 31, 53–79]	Table 6
Dwarf spheroidal galaxies	11	[16, 79–83]	Table 5
total	357		

Supplementary Table 1: **Observational data.** The table lists the types of objects; references used to collect the observational data; and the final list of selected objects.



Supplementary Figure 7: **DM Column density as a function of the halo mass.** Similar to the Figure 1, we plot 289 objects, selected in Section B above (coloured shapes) superimposed on the simulation data for isolated halos [6] (open black circles).

Supplementary Table 3: Halo mass M_{200} and DM column density \mathcal{S} for galaxy groups.

Object name	$M_{200}[M_{\odot}]$	$\log_{10} \frac{\mathcal{S}}{M_{\odot} \text{ pc}^{-2}}$	Object name	$M_{200}[M_{\odot}]$	$\log_{10} \frac{\mathcal{S}}{M_{\odot} \text{ pc}^{-2}}$
Abell 1275	8.20e+13	2.57	Abell 1692	1.09e+14	2.77
Abell 2462	1.11e+14	2.51	Abell 2550	8.93e+13	2.64
Abell 3880	2.03e+14	2.69	ESO 306-G017 (group)	1.74e+14	2.73
ESO 351-G021 (group)	3.66e+13	2.18	ESO 552-G020 (group)	1.31e+14	2.60
IC 1860 (group)	5.02e+13	2.58	MKW 4	5.97e+13	2.68
NGC 1407 (group)	6.13e+13	2.52	NGC 1550 (group)	3.61e+13	2.73
NGC 2563 (group)	2.51e+13	2.51	NGC 4104 (group)	6.18e+13	2.55
NGC 4325 (group)	3.57e+13	2.64	NGC 5044 (group)	3.67e+13	2.64
NGC 5098 (group)	2.52e+13	2.42	NGC 5129 (group)	1.51e+13	2.69
NGC 533 (group)	2.31e+13	2.84	RGH 80	2.80e+13	2.53
RX J1022.1+3830	1.00e+14	2.58	RX J1158.1+5521	1.05e+14	2.43
RX J1159.8+5531	8.33e+13	2.75	UGC 5088 (group)	1.93e+13	2.36
UGC 842 (group)	7.00e+13	2.77			
Galaxy Groups					

 Supplementary Table 4: Halo mass M_{200} and DM column density \mathcal{S} for elliptical galaxies.

Object name	$M_{200}[M_{\odot}]$	$\log_{10} \frac{\mathcal{S}}{M_{\odot} \text{ pc}^{-2}}$	Object name	$M_{200}[M_{\odot}]$	$\log_{10} \frac{\mathcal{S}}{M_{\odot} \text{ pc}^{-2}}$
M49 (NGC 4472)	2.85e+13	2.67	M60 (NGC 4649)	3.05e+13	2.99
NGC 4125	5.32e+12	2.26	NGC 4261	4.77e+13	2.01
NGC 6482	6.12e+12	2.64	NGC 720	5.43e+12	2.63
Elliptical galaxies					

 Supplementary Table 5: Halo mass M_{200} and DM column density \mathcal{S} for dwarf spheroidal galaxies (dSphs).

Object name	$M_{200}[M_{\odot}]$	$\log_{10} \frac{\mathcal{S}}{M_{\odot} \text{ pc}^{-2}}$	Object name	$M_{200}[M_{\odot}]$	$\log_{10} \frac{\mathcal{S}}{M_{\odot} \text{ pc}^{-2}}$
Carina	2.63e+09	1.64	Coma Berenices	1.00e+08	1.85
Draco	1.25e+09	1.97	Fornax	3.04e+09	1.54
Leo II	7.17e+08	1.69	Ursa Major II	1.27e+08	1.83
Ursa Minor	1.85e+09	2.01	Willman I	7.61e+07	1.98
Dwarf spheroidal galaxies					

Supplementary Table 6: Halo mass M_{200} and DM column density \mathcal{S} for spiral, low-surface brightness (LSB) and dwarf galaxies (without dSphs).

Object name	$M_{200}[M_{\odot}]$	$\log_{10} \frac{\mathcal{S}}{M_{\odot} \text{ pc}^{-2}}$	Object name	$M_{200}[M_{\odot}]$	$\log_{10} \frac{\mathcal{S}}{M_{\odot} \text{ pc}^{-2}}$
DDO 154	5.52e+10	1.44	DDO 170	6.82e+10	1.60
DDO 189	4.26e+10	1.85	DDO 47	2.13e+11	2.03
DDO 52	2.00e+10	1.89	DDO 64	5.28e+10	1.89
ESO 116-G12	5.14e+10	1.65	ESO 287-G13	1.36e+09	0.95
ESO 79-G14	4.41e+08	1.08	IC 1401	1.54e+12	1.31
IC 2574	2.28e+11	1.59	KK 98250	4.57e+10	1.70
LSBC F563-1	2.78e+11	1.95	LSBC F563-v2	2.41e+11	2.10
LSBC F568-1	4.35e+11	2.28	LSBC F568-3	4.66e+11	1.89
LSBC F568-v1	2.37e+11	2.25	LSBC F571-8	5.74e+11	2.25
LSBC F574-1	2.15e+11	2.05	LSBC F583-1	2.56e+11	1.75
LSBC F583-4	9.37e+10	1.82	M31	8.30e+11	2.63
M33 (NGC 598)	6.48e+11	1.93	Milky Way	1.03e+12	2.40
NGC 100	2.50e+11	2.04	NGC 1003	5.30e+11	1.48
NGC 1085	4.37e+12	2.35	NGC 1087	7.06e+11	2.10
NGC 1090	3.01e+08	1.06	NGC 1353	1.27e+12	2.34
NGC 1421	1.60e+12	1.93	NGC 1560	7.91e+11	1.67
NGC 224	1.18e+13	1.97	NGC 2366	2.51e+10	1.79
NGC 2403	3.80e+11	2.11	NGC 247	4.47e+12	1.88
NGC 2532	4.39e+11	2.18	NGC 2537	7.85e+10	2.29
NGC 2552	1.44e+12	2.38	NGC 2608	3.10e+11	1.94
NGC 2708	1.86e+12	2.63	NGC 2841	1.87e+12	2.66
NGC 2903	6.96e+11	2.43	NGC 2977	4.54e+11	2.47
NGC 300	8.95e+11	1.87	NGC 3026	1.39e+12	2.43
NGC 3031	2.52e+11	2.70	NGC 3109	1.16e+11	1.30
NGC 3198	3.64e+11	2.04	NGC 3200	2.16e+12	2.53
NGC 3274	5.50e+10	2.46	NGC 3319	8.11e+11	1.74
NGC 3346	4.04e+11	2.50	NGC 3495	1.68e+13	3.33
NGC 3521	5.80e+11	2.15	NGC 3621	6.05e+11	1.93
NGC 3741	1.99e+10	1.73	NGC 3893	1.98e+12	2.84
NGC 3898	9.42e+12	2.48	NGC 4190	5.20e+11	1.59
NGC 4236	1.95e+11	1.73	NGC 4242	1.08e+12	1.80
NGC 4258	3.04e+12	1.92	NGC 4288	1.00e+11	2.26
NGC 4395	6.40e+10	2.06	NGC 4455	1.00e+11	1.78
NGC 4494	8.65e+11	1.87	NGC 45	8.25e+11	1.97
NGC 4605	1.06e+11	2.33	NGC 4635	5.21e+11	2.53
NGC 4736	2.30e+11	2.48	NGC 4800	3.51e+11	2.70
NGC 5023	1.35e+11	2.14	NGC 5033	1.25e+12	1.93
NGC 5055	2.17e+12	1.86	NGC 5194	1.56e+12	2.82
NGC 5204	9.53e+10	2.15	NGC 55	1.00e+12	1.73
NGC 5585	3.40e+11	1.85	NGC 5608	4.97e+10	1.68
NGC 5727	5.41e+12	2.06	NGC 5949	1.72e+11	2.33
NGC 5963	6.08e+11	1.76	NGC 6015	1.25e+12	2.49
NGC 6503	6.90e+11	1.98	NGC 6682	5.22e+10	1.78
NGC 6689	2.76e+11	2.12	NGC 6946	6.19e+12	2.06
NGC 7137	4.45e+10	2.12	NGC 7217	2.47e+12	2.69
NGC 7339	3.54e+11	1.89	NGC 753	1.92e+12	1.82
NGC 7541	2.52e+12	2.17	NGC 7664	1.26e+12	2.03
NGC 7793	3.68e+11	2.16	NGC 925	6.16e+11	1.81
NGC 959	4.87e+10	2.60	UGC 02259	9.49e+11	1.76
UGC 10310	1.81e+11	1.71	UGC 11557	4.47e+11	1.84
UGC 11707	2.11e+11	2.03	UGC 11820	1.99e+11	2.43
UGC 11861	8.14e+11	2.21	UGC 12060	5.37e+11	1.98
UGC 1230	1.47e+11	2.01	UGC 12632	4.55e+10	1.92
UGC 12732	1.47e+11	1.81	UGC 128	3.84e+11	2.08
UGC 1281	9.96e+10	1.74	UGC 12810	1.78e+12	2.40
UGC 1551	4.98e+10	1.82	UGC 2259	5.37e+10	2.35

Spiral, LSB and dwarf galaxies (without dSphs) (continued on next page)

Object name	$M_{200}[M_{\odot}]$	$\log_{10} \frac{S}{M_{\odot} \text{ pc}^{-2}}$	Object name	$M_{200}[M_{\odot}]$	$\log_{10} \frac{S}{M_{\odot} \text{ pc}^{-2}}$
UGC 2885	8.22e+12	1.86	UGC 3137	2.10e+11	2.02
UGC 3371	1.81e+11	1.75	UGC 4173	4.62e+10	1.23
UGC 4499	1.03e+11	1.85	UGC 477	4.00e+11	1.98
UGC 5005	4.52e+11	1.54	UGC 5750	2.50e+11	1.46
UGC 628	2.73e+11	2.23	UGC 6446	5.83e+10	1.84
UGC 731	4.42e+10	2.13	UGC 7699	1.44e+11	1.70
UGC 9211	2.84e+10	1.99			
Spiral, LSB and dwarf galaxies (without dSphs) (<i>end</i>)					

References

- [1] Evrard, A. E., Metzler, C. A. & Navarro, J. F. Mass Estimates of X-Ray Clusters. *ApJ* **469**, 494 (1996). [astro-ph/9510058](#).
- [2] Buote, D. A. X-Ray Constraints on Dark Matter in Galaxy Clusters and Elliptical Galaxies: A View from Chandra and XMM. In S. Ryder, D. Pisano, M. Walker, & K. Freeman (ed.) *Dark Matter in Galaxies*, vol. 220 of *IAU Symposium*, 149–+ (2004). [astro-ph/0310579](#).
- [3] Refregier, A. Weak Gravitational Lensing by Large-Scale Structure. *ARA&A* **41**, 645–668 (2003). [astro-ph/0307212](#).
- [4] Bergstrom, L. Non-baryonic dark matter - observational evidence and detection methods. *Rept.Prog.Phys.* **63**, 793 (2000). [hep-ph/0002126](#).
- [5] Neto, A. F. *et al.* The statistics of Λ CDM halo concentrations. *MNRAS* **381**, 1450–1462 (2007). [0706.2919](#).
- [6] Macciò, A. V., Dutton, A. A. & van den Bosch, F. C. Concentration, spin and shape of dark matter haloes as a function of the cosmological model: WMAP1, WMAP3 and WMAP5 results. *MNRAS* **391**, 1940–1954 (2008). [0805.1926](#).
- [7] Springel, V. *et al.* The Aquarius Project: the subhaloes of galactic haloes. *MNRAS* **391**, 1685–1711 (2008). [0809.0898](#).
- [8] Kormendy, J. & Freeman, K. C. Scaling Laws for Dark Matter Halos in Late-Type and Dwarf Spheroidal Galaxies. In S. Ryder, D. Pisano, M. Walker, & K. Freeman (ed.) *Dark Matter in Galaxies*, vol. 220 of *IAU Symposium*, 377–+ (2004).
- [9] Donato, F. *et al.* A constant dark matter halo surface density in galaxies. *MNRAS* **397**, 1169–1176 (2009). [0904.4054](#).
- [10] Gentile, G., Famaey, B., Zhao, H. & Salucci, P. Universality of galactic surface densities within one dark halo scale-length. *Nature* **461**, 627 (2009). [0909.5203](#).
- [11] Komatsu, E. *et al.* Five-Year Wilkinson Microwave Anisotropy Probe (WMAP) Observations: Cosmological Interpretation. *Astrophys. J. Suppl.* **180**, 330–376 (2009). [0803.0547](#).
- [12] Bertschinger, E. Simulations of structure formation in the universe. *Ann. Rev. Astron. Astrophys.* **36**, 599–654 (1998).
- [13] Navarro, J. F., Frenk, C. S. & White, S. D. M. A universal density profile from hierarchical clustering. *ApJ* **490**, 493–508 (1997). [astro-ph/9611107](#).

- [14] Stadel, J. *et al.* Quantifying the heart of darkness with GHALO - a multibillion particle simulation of a galactic halo. *MNRAS* **398**, L21–L25 (2009). 0808.2981.
- [15] Burkert, A. The Structure of Dark Matter Halos in Dwarf Galaxies. *ApJ* **447**, L25+ (1995). astro-ph/9504041.
- [16] Gilmore, G. *et al.* The Observed Properties of Dark Matter on Small Spatial Scales. *ApJ* **663**, 948–959 (2007). astro-ph/0703308.
- [17] Gentile, G., Tonini, C. & Salucci, P. LambdaCDM Halo Density Profiles: where do actual halos converge to NFW ones? *Astron. Astrophys.* **467**, 925–931 (2007). astro-ph/0701550.
- [18] Kent, S. M. Dark matter in spiral galaxies. I - Galaxies with optical rotation curves. *AJ* **91**, 1301–1327 (1986).
- [19] Goerdt, T., Moore, B., Read, J. I., Stadel, J. & Zemp, M. Does the fornax dwarf spheroidal have a central cusp or core? *MNRAS* **368**, 1073–1077 (2006). astro-ph/0601404.
- [20] Sánchez-Salcedo, F. J., Reyes-Iturbide, J. & Hernandez, X. An extensive study of dynamical friction in dwarf galaxies: the role of stars, dark matter, halo profiles and MOND. *MNRAS* **370**, 1829–1840 (2006). astro-ph/0601490.
- [21] de Blok, W. J. G. The Core-Cusp Problem. *Advances in Astrophysics* (2009). 0910.3538.
- [22] Boyarsky, A., Neronov, A., Ruchayskiy, O., Shaposhnikov, M. & Tkachev, I. How to find a dark matter sterile neutrino? *Phys. Rev. Lett.* **97**, 261302 (2006). astro-ph/0603660.
- [23] Bullock, J. S. *et al.* Profiles of dark haloes: evolution, scatter and environment. *MNRAS* **321**, 559–575 (2001). astro-ph/9908159.
- [24] Bode, P., Ostriker, J. P. & Turok, N. Halo formation in warm dark matter models. *ApJ* **556**, 93–107 (2001). astro-ph/0010389.
- [25] Dvali, G. R., Gabadadze, G. & Porrati, M. 4D gravity on a brane in 5D Minkowski space. *Phys. Lett.* **B485**, 208–214 (2000). hep-th/0005016.
- [26] Kormendy, J. & Djorgovski, S. Surface photometry and the structure of elliptical galaxies. *ARA&A* **27**, 235–277 (1989).
- [27] Tully, R. B. & Fisher, J. R. A new method of determining distances to galaxies. *A&A* **54**, 661–673 (1977).
- [28] Milgrom, M. A Modification of the Newtonian dynamics as a possible alternative to the hidden mass hypothesis. *Astrophys. J.* **270**, 365–370 (1983).
- [29] Bertone, G., Buchmuller, W., Covi, L. & Ibarra, A. Gamma-rays from decaying dark matter. *JCAP* **0711**, 003 (2007). 0709.2299.
- [30] Boyarsky, A., Ruchayskiy, O. & Shaposhnikov, M. The role of sterile neutrinos in cosmology and astrophysics. *Ann. Rev. Nucl. Part. Sci.* **59**, 191 (2009). 0901.0011.
- [31] Gentile, G., Salucci, P., Klein, U., Vergani, D. & Kalberla, P. The cored distribution of dark matter in spiral galaxies. *MNRAS* **351**, 903–922 (2004). astro-ph/0403154.
- [32] Bardeau, S. *et al.* A CFH12k lensing survey of X-ray luminous galaxy clusters. II. Weak lensing analysis and global correlations. *A&A* **470**, 449–466 (2007). astro-ph/0703395.

- [33] Broadhurst, T., Umetsu, K., Medezinski, E., Oguri, M. & Rephaeli, Y. Comparison of Cluster Lensing Profiles with Λ CDM Predictions. *ApJ* **685**, L9–L12 (2008). 0805.2617.
- [34] Comerford, J. M. & Natarajan, P. The observed concentration-mass relation for galaxy clusters. *MNRAS* **379**, 190–200 (2007). astro-ph/0703126.
- [35] Corless, V. L., King, L. J. & Clowe, D. A new look at massive clusters: weak lensing constraints on the triaxial dark matter haloes of A1689, A1835 and A2204. *MNRAS* **393**, 1235–1254 (2009). 0812.0632.
- [36] Donnarumma, A., Ettori, S., Meneghetti, M. & Moscardini, L. X-ray and strong lensing mass estimate of MS2137.3-2353. *MNRAS* **398**, 438–450 (2009). 0902.4051.
- [37] Ettori, S., De Grandi, S. & Molendi, S. Gravitating mass profiles of nearby galaxy clusters and relations with X-ray gas temperature, luminosity and mass. *A&A* **391**, 841–855 (2002). astro-ph/0206120.
- [38] Gavazzi, R. *et al.* A weak lensing study of the Coma cluster. *A&A* **498**, L33–L36 (2009). 0904.0220.
- [39] Kubo, J. M. *et al.* The Mass of the Coma Cluster from Weak Lensing in the Sloan Digital Sky Survey. *ApJ* **671**, 1466–1470 (2007). 0709.0506.
- [40] McLaughlin, D. E. Evidence in Virgo for the Universal Dark Matter Halo. *ApJ* **512**, L9–L12 (1999). astro-ph/9812242.
- [41] Rines, K., Geller, M. J., Kurtz, M. J. & Diaferio, A. CAIRNS: The Cluster and Infall Region Nearby Survey. I. Redshifts and Mass Profiles. *AJ* **126**, 2152–2170 (2003). astro-ph/0306538.
- [42] Schmidt, R. W. & Allen, S. W. The dark matter haloes of massive, relaxed galaxy clusters observed with Chandra. *MNRAS* **379**, 209–221 (2007). astro-ph/0610038.
- [43] Sereno, M., Lubini, M. & Jetzer, P. A multi-wavelength strong lensing analysis of baryons and dark matter in the dynamically active cluster AC 114. *ArXiv e-prints* (2009). 0904.0018.
- [44] Umetsu, K. & Broadhurst, T. Combining Lens Distortion and Depletion to Map the Mass Distribution of A1689. *ApJ* **684**, 177–203 (2008). 0712.3441.
- [45] Gastaldello, F. *et al.* Probing the Dark Matter and Gas Fraction in Relaxed Galaxy Groups with X-Ray Observations from Chandra and XMM-Newton. *ApJ* **669**, 158–183 (2007). astro-ph/0610134.
- [46] Romanowsky, A. J. *et al.* Mapping The Dark Side with DEIMOS: Globular Clusters, X-Ray Gas, and Dark Matter in the NGC 1407 Group. *AJ* **137**, 4956–4987 (2009). 0809.2088.
- [47] Sun, M. *et al.* Chandra Studies of the X-Ray Gas Properties of Galaxy Groups. *ApJ* **693**, 1142–1172 (2009). 0805.2320.
- [48] Humphrey, P. J. *et al.* A Chandra View of Dark Matter in Early-Type Galaxies. *ApJ* **646**, 899–918 (2006). astro-ph/0601301.
- [49] Weijmans, A.-M. *et al.* The shape of the dark matter halo in the early-type galaxy NGC 2974. *MNRAS* **383**, 1343–1358 (2008). 0711.1775.
- [50] Weijmans, A. *et al.* Stellar velocity profiles and line strengths out to four effective radii in the early-type galaxies NGC3379 and 821. *MNRAS* **398**, 561–574 (2009). 0906.0018.

- [51] Napolitano, N. R. *et al.* The Planetary Nebula Spectrograph elliptical galaxy survey: the dark matter in NGC 4494. *MNRAS* **393**, 329–353 (2009). 0810.1291.
- [52] Zhang, Z. *et al.* Probing the Mass Distributions in NGC 1407 and Its Associated Group with the X-Ray Imaging Spectroscopic and Optical Photometric and Line-Strength Indices Data. *ApJ* **656**, 805–817 (2007). astro-ph/0610934.
- [53] Athanassoula, E., Bosma, A. & Papaioannou, S. Halo parameters of spiral galaxies. *A&A* **179**, 23–40 (1987).
- [54] Battaglia, G. *et al.* The radial velocity dispersion profile of the galactic halo: Constraining the density profile of the dark halo of the milky way. *Mon. Not. Roy. Astron. Soc.* **364**, 433–442 (2005). astro-ph/0506102.
- [55] Begeman, K. G., Broeils, A. H. & Sanders, R. H. Extended rotation curves of spiral galaxies - Dark haloes and modified dynamics. *MNRAS* **249**, 523–537 (1991).
- [56] Begum, A. & Chengalur, J. N. Kinematics of two dwarf galaxies in the NGC 6946 group. *A&A* **424**, 509–517 (2004).
- [57] Blais-Ouellette, S., Carignan, C., Amram, P. & Côté, S. Accurate Parameters of the Mass Distribution in Spiral Galaxies. I. Fabry-Perot Observations of NGC 5585. *AJ* **118**, 2123–2131 (1999). astro-ph/9911223.
- [58] de Blok, W. J. G. & Bosma, A. High-resolution rotation curves of low surface brightness galaxies. *A&A* **385**, 816–846 (2002). astro-ph/0201276.
- [59] de Blok, W. J. G. *et al.* High-Resolution Rotation Curves and Galaxy Mass Models from Things. *AJ* **136**, 2648–2719 (2008). 0810.2100.
- [60] de Blok, W. J. G. & McGaugh, S. S. The dark and visible matter content of low surface brightness disc galaxies. *MNRAS* **290**, 533–552 (1997). astro-ph/9704274.
- [61] van den Bosch, F. C. & Swaters, R. A. Dwarf galaxy rotation curves and the core problem of dark matter haloes. *MNRAS* **325**, 1017–1038 (2001). astro-ph/0006048.
- [62] Chemin, L., Carignan, C., Drouin, N. & Freeman, K. C. H I Studies of the Sculptor Group Galaxies. VIII. The Background Galaxies: NGC 24 and NGC 45. *AJ* **132**, 2527–2538 (2006). astro-ph/0609148.
- [63] Côté, S., Carignan, C. & Freeman, K. C. The Various Kinematics of Dwarf Irregular Galaxies in Nearby Groups and Their Dark Matter Distributions. *AJ* **120**, 3027–3059 (2000).
- [64] Cote, S., Carignan, C. & Sancisi, R. A dark-halo-dominated galaxy - NGC 5585. *AJ* **102**, 904–913 (1991).
- [65] Dutton, A. A., Courteau, S., de Jong, R. & Carignan, C. Mass Modeling of Disk Galaxies: Degeneracies, Constraints, and Adiabatic Contraction. *ApJ* **619**, 218–242 (2005). astro-ph/0310001.
- [66] Geehan, J. J., Fardal, M. A., Babul, A. & Guhathakurta, P. Investigating the Andromeda stream - I. Simple analytic bulge-disc-halo model for M31. *MNRAS* **366**, 996–1011 (2006). astro-ph/0501240.

- [67] Kent, S. M. Dark matter in spiral galaxies. II - Galaxies with H I rotation curves. *AJ* **93**, 816–832 (1987).
- [68] Lake, G. & Feinswog, L. The distribution of dark matter in galaxies. I - Models of spiral galaxies. *AJ* **98**, 166–179 (1989).
- [69] Lake, G., Schommer, R. A. & van Gorkom, J. H. The distribution of dark matter in the dwarf galaxy DDO 170. *AJ* **99**, 547–560 (1990).
- [70] Marchesini, D. *et al.* H α Rotation Curves: The Soft Core Question. *ApJ* **575**, 801–813 (2002). [astro-ph/0202075](#).
- [71] Kuzio de Naray, R., McGaugh, S. S., de Blok, W. J. G. & Bosma, A. High-Resolution Optical Velocity Fields of 11 Low Surface Brightness Galaxies. *ApJS* **165**, 461–479 (2006). [astro-ph/0604576](#).
- [72] Kuzio de Naray, R., McGaugh, S. S. & de Blok, W. J. G. Mass Models for Low Surface Brightness Galaxies with High-Resolution Optical Velocity Fields. *ApJ* **676**, 920–943 (2008). 0712.0860.
- [73] Puche, D. & Carignan, C. H I studies of the Sculptor group galaxies. VII - Implications on the distribution and nature of dark matter in groups. *ApJ* **378**, 487–495 (1991).
- [74] Sicotte, V. & Carignan, C. NGC 5204: A Strongly Warped Magellanic Spiral.II.H I Kinematics and Mass Distribution. *AJ* **113**, 609–617 (1997).
- [75] Spano, M. *et al.* GHASP: an H α kinematic survey of spiral and irregular galaxies - V. Dark matter distribution in 36 nearby spiral galaxies. *MNRAS* **383**, 297–316 (2008). 0710.1345.
- [76] Swaters, R. A., Madore, B. F., van den Bosch, F. C. & Balcells, M. The Central Mass Distribution in Dwarf and Low Surface Brightness Galaxies. *ApJ* **583**, 732–751 (2003). [astro-ph/0210152](#).
- [77] Tempel, E., Tamm, A. & Tenjes, P. Visible and dark matter in M 31 - II. A dynamical model and dark matter density distribution **707** (2007). 0707.4374.
- [78] Weldrake, D. T. F., de Blok, W. J. G. & Walter, F. A high-resolution rotation curve of NGC 6822: a test-case for cold dark matter. *MNRAS* **340**, 12–28 (2003). [astro-ph/0210568](#).
- [79] Frigerio Martins, C. The distribution of the dark matter in galaxies as the imprint of its Nature. *ArXiv e-prints* (2009). 0903.4588.
- [80] Strigari, L. E. *et al.* Redefining the Missing Satellites Problem. *ApJ* **669**, 676–683 (2007). 0704.1817.
- [81] Wu, X. The mass distribution of dwarf spheroidal galaxies from stellar kinematics: Draco, Ursa Minor and Fornax. *ArXiv Astrophysics e-prints* (2007). [astro-ph/0702233](#).
- [82] Walker, M. G. *et al.* A Universal Mass Profile for Dwarf Spheroidal Galaxies. *ApJ* **704**, 1274–1287 (2009). 0906.0341.
- [83] van Eymeren, J., Trachternach, C., Koribalski, B. S. & Dettmar, R. Non-circular motions and the cusp-core discrepancy in dwarf galaxies. *A&A* **505**, 1–20 (2009). 0906.4654.